Reserved-Energy-Aided Control in Solid-State Transformers

Radhika Sarda, *Graduate Student Member, IEEE*, Ezequiel Rodriguez Ramos, *Member, IEEE*, Glen G. Farivar, *Senior Member, IEEE*, Josep Pou, *Fellow, IEEE*, Howe Li Yeo, Vaisambhayana B. Sriram, *Member, IEEE*, and Anshuman Tripathi

***Abstract*—Solid-state transformers (SSTs) operate within the overvoltage and undervoltage limits to ensure safety and power quality (prevent overmodulation). This constrained region of operation creates a reserve of available energy in the system, which is primarily stored in the multiple dc-link capacitors. The energy reserves in the system are essential during load transients as the initial energy demand is compensated by the dc-link capacitors. This article presents a detailed analysis of the energy distribution during load transients for different SST control strategies and the impact of control gains. Subsequently, a reserved-energy-aided control parameter design approach is proposed that effectively distributes the stored energy of the capacitors within prescribed operating limits for a safe and controllable operation. The proposed design approach expands the operational range of SSTs, allowing them to handle larger variations in load power compared to conventional control design strategies. The results are validated on a single-phase, two-stage, two-string 230-V/250-V 1-kVA 50-kHz SST system.**

***Index Terms*—Energy distribution, load transient, solid-state transformers (SSTs), stability.**

I. Introduction

RESEARCHERS are exploring replacing conventional passive transformers in distribution systems with more advanced solid-state transformer (SST) solutions [1], [2], [3]. In addition to the flexibility in control, SSTs also provide grid quality support, availability of dc ports, isolation of faults, reduced weight, and volume of transformers, etc. [1], [2], [3]. The development of high-voltage (HV) high-power SSTs is benefiting from advancements in wide bandgap devices and high-frequency magnetics, allowing for modular designs [2], [4], [5], [6], [7], [8]. The most commonly used architecture for the SST involves three-stage conversion, as shown in Fig. 1, due to its ease of scalability and modularity [9], [10]. The ac–dc conversion unit can be realised with a cascaded H-bridge (CHB) topology, forming the Stage I. Dual-active bridges (DABs) interface the HV and low-voltage (LV) dc-link capacitors, forming the Stage II. Finally, Stage III consists of a two-level inverter interfacing the LV grid.

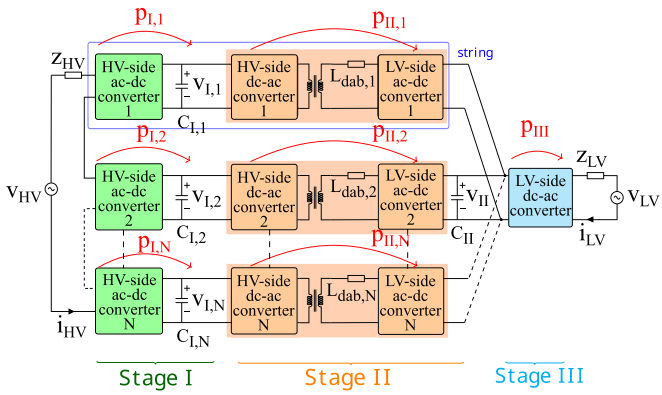

Fig. 1. Single-phase three-stage architecture of an SST.

With substantial decoupling between stages provided by large dc-link capacitors, each stage of the SST can be designed with specific and independent control objectives. While all stages must regulate their respective power flows to maintain stable dc-link voltages, Stages I and III are also responsible for ensuring respective grid current, and Stage II typically focuses on balancing the HV dc-link capacitor voltages [2], [11], [12], [13]. The objectives are often achieved with nested control loops. The inner current control loops of all the stages usually employ conventional proportional–integral (PI) or resonant controllers. The outer capacitor voltage (or energy) control loops, which regulate the capacitor voltages to preset values by shaping the current (or power) references used in the inner control loops of Stages I and II, also commonly employ PI controllers [13]. In the literature, the outer control loops are designed using either capacitor voltages or squared capacitor voltages (proportional to capacitor energy). In this article, energy variables are assumed, given the linear relationship between energy and power [14], [15]. Besides, this article assumes that the load (the active

Received 5 August 2024; revised 6 November 2024 and 5 January 2025; accepted 24 February 2025. Date of publication 3 March 2025; date of current version 14 April 2025. Recommended for publication by Associate Editor J. He. *(Corresponding author: Radhika Sarda.)*

Radhika Sarda is with the Energy Research Institute@ NTU, Interdisciplinary Graduate Programme, Nanyang Technological University, Singapore 639798 (e-mail: radhika010@e.ntu.edu.sg).

Ezequiel Rodriguez Ramos, Howe Li Yeo, Vaisambhayana B. Sriram, and Anshuman Tripathi are with the Energy Research Institute, Nanyang Technological University, Singapore 639798 (e-mail: ezequiel001@e.ntu.edu.sg; hlyeo@ntu.edu.sg; vsriram@ntu.edu.sg; ANTRI@ntu.edu.sg).

Glen G. Farivar is with the Department of Electrical and Electronic Engineering, University of Melbourne, Melbourne, VIC 3010, Australia (e-mail: gfarivar@unimelb.edu.au).

Josep Pou is with the Department of Electrical Engineering, City University of Hong Kong, Hong Kong SAR 999077, China (e-mail: josep.pou@ieee.org).

Color versions of one or more figures in this article are available at https://doi.org/10.1109/TPEL.2025.3547155.

Digital Object Identifier 10.1109/TPEL.2025.3547155

power requirement from Stage III) is unknown, and thus load feedforward signal is unavailable for control purposes.

During a load transient event, the dc-link capacitor voltages deviate from their references, indicating an imbalance in power flow, that should be compensated by the source. Various combinations of the dc-link capacitor voltages (energies) variations can be used as control state variables for the aforementioned outer voltage (energy) loops to create new steady-state power references. In [11], [12], [13], [16], Stage I controls the sum of the HV-side capacitor voltages (energies), while Stage II regulates the LV-side capacitor voltage (energy), referred to as conventional control (CC) in the sequel. In [15], Stage I's role shifts to regulate the total stored energy within the SST. This decouples the control, simplifying its synthesis, and it is termed decoupled control (DC). In [17], Stage II's responsibility shifts to control the energy difference between the LV-side capacitor and each HV-side capacitor (Stage I maintains its role of controlling the total stored energy). This ensures equal distribution of transient energy across all the capacitors, regardless of control gains, and is referred as balanced control (BC). Note that, among the reported SST control strategies in the literature, CC is the most widely used. Other more advanced control strategies [18], [19], [20], [21], such as the use of artificial neural networks or model predictive control, still fall within the CC strategy given the choice of state variables adopted.

Although the CC, DC, and BC strategies can be designed to ensure theoretically stable closed-loop systems, ensuring operational stability, i.e., avoiding unsafe or nonlinear operation that can lead to instability, requires the voltage (energy) variables of the capacitors to be confined within the prescribed regions. For example, the voltage on each of the HV side capacitors must be above the peak value of its reference voltage on the ac side to avoid overmodulation and, at the same time, remain below a maximum limit that defines the safe area of operation. This article analytically evaluates the suitability of the CC, DC, and BC strategies to guarantee capacitor voltage operation within prescribed limits, and examines the impact of the control gains. Furthermore, by introducing the concept of energy reserves, the article proposes a control design approach that extends the stable region of the SST, accommodating large load variations.

The rest of this article is organized as follows. In Section II, the architecture of the SST and the CC strategies are discussed. Section III reveals an in-depth analysis of the energy distribution during load transients, comparing conventional, and alternative control methods previously reported for SSTs. Section IV introduces a reserved-energy-based control design approach that effectively harnesses the reserve dc-link capacitor energies. Sections V presents the experimental results that assess the accuracy of the proposed analysis and control design approach. Finally, Section VI concludes this article.

II. SST Control Strategies – Background

This section provides an overview of the single-phase three-stage SST structure shown in Fig. 1 and different control strategies.

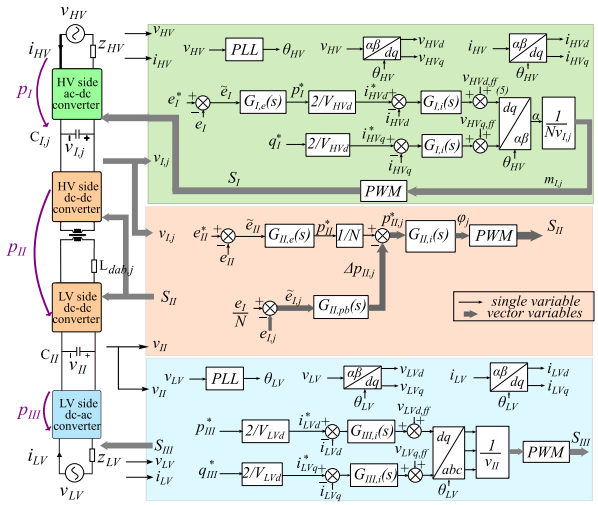

Fig. 2. CC of the SST in Stages I, II, and III.

A. Architecture and Main Variables

In the circuit diagram of a single-phase three-stage SST in Fig. 1, the HV-side is characterized by voltage, $v_{\rm HV}$, current, $i_{\rm HV}$, and impedance $Z_{\rm HV} = R_{\rm HV} + j\omega_{\rm HV}L_{\rm HV}$. Similarly, LV-side is characterized by voltage, $v_{\rm LV}$, current, $i_{\rm LV}$, and impedance $Z_{\rm LV} = R_{\rm LV} + j\omega_{\rm LV}L_{\rm LV}$. Parameters $\omega_{\rm HV}$, $\omega_{\rm LV}$, $R_{\rm HV}$, $R_{\rm LV}$, $L_{\rm HV}$, and $L_{\rm LV}$ denote the grid angular frequency, the parasitic resistance, and the inductance, at the HV and LV sides, respectively. Each phase consists of N strings and $j \in \{1, 2, \ldots, N\}$ refers to the string index. The power transfer through each DAB is facilitated by using external inductance represented as $L_{{\rm dab},j}$ in Fig. 1. The HV dc-link capacitor of the jth string, $C_{{\rm I},j}$, holds voltage, $v_{{\rm I},j}$, whereas the LV dc-link capacitor, $C_{\rm II}$, holds voltage, $v_{\rm II}$. Variables $p_{{\rm I},j}$ and $p_{{\rm II},j}$ are the instantaneous powers flowing through the jth string of Stage I and Stage II, respectively, while $p_{\rm III}$ refers to the instantaneous power flowing through Stage III. The HV and LV dc-link energy variables correspond to, respectively

$$e_{{\rm I},j} = \frac{1}{2}C_{{\rm I},j}v_{{\rm I},j}^2 \tag{1}$$

$$e_{\rm II} = \frac{1}{2}C_{\rm II}v_{\rm II}^2. \tag{2}$$

In addition, the total HV dc-link energy and the total SST dc-link energy correspond to, respectively,

$$e_I = \sum_{j=1}^{N} e_{{\rm I},j} \tag{3}$$

$$e_\Sigma = e_I + e_{\rm II}. \tag{4}$$

B. Control Strategies

The CC strategy is illustrated in Fig. 2, and discussed next. Note that a single string has been used for the sake of illustration. Other notable work with different control variables are also proposed for SSTs, which is considered subsequently for comparison.

TABLE I
CONTROL LAWS FOR DIFFERENT SST CONTROL STRATEGIES

Control	Control Laws	
	Stage I	Stage II
Conventional [13]	$\tilde{p}_I = -\alpha_1 \tilde{e}_I - \alpha_2 \int \tilde{e}_{II}$	$\tilde{p}_{II,j} = -\frac{1}{N}(\beta_1 \tilde{e}_{II} + \beta_2 \int \tilde{e}_{II}) + \Delta p_{II,j}$ $\Delta p_{II,j} = -\xi_1(\frac{\tilde{e}_I}{N} - \tilde{e}_{I,j}) - \xi_2 \int (\frac{\tilde{e}_I}{N} - \tilde{e}_{I,j})$
Decoupled [15]	$\tilde{p}_I = -\alpha_1 \tilde{e}_\Sigma - \alpha_2 \int \tilde{e}_\Sigma$	$\tilde{p}_{II,j} = -\frac{1}{N}(\beta_1 \tilde{e}_{II} + \beta_2 \int \tilde{e}_{II}) + \Delta p_{II,j}$ $\Delta p_{II,j} = -\xi_1(\frac{\tilde{e}_I}{N} - \tilde{e}_{I,j}) - \xi_2 \int (\frac{\tilde{e}_I}{N} - \tilde{e}_{I,j})$
Balanced [17]	$\tilde{p}_I = -\alpha_1 \tilde{e}_\Sigma - \alpha_2 \int \tilde{e}_\Sigma$	$\tilde{p}_{II,j} = -\beta_1(\tilde{e}_{II} - \tilde{e}_{I,j}) - \beta_2 \int (\tilde{e}_{II} - \tilde{e}_{I,j})$

1) CC: (a) Stage-I control: The main objectives of Stage I are (i) to regulate the HV-side active and reactive powers, p_I and q_I, to their corresponding prescribed reference values, $p_{\rm I}^*$ and $q_{\rm I}^*$, while (ii) regulating the dc component of e_I to the prescribed reference e_I^*. Note that the control objective (ii) is achieved by modifying the active power reference $p_{\rm I}^*$ used in the control objective (i). The control objective (i) is achieved via a dq-frame current control loop, where feedforward and decoupling terms are embedded in variables $v_{{\rm HV}d,ff}$ and $v_{{\rm HV}q,ff}$, as

$$\begin{aligned} v_{{\rm HV}d,ff} &= v_{{\rm HV}d} + \omega_{\rm HV} L_{\rm HV} i_{{\rm HV}q} \\ v_{{\rm HV}q,ff} &= v_{{\rm HV}q} - \omega_{\rm HV} L_{\rm HV} i_{{\rm HV}d} \end{aligned} \tag{5}$$

$\{v_{{\rm HV}d}, v_{{\rm HV}q}\}$ and $\{i_{{\rm HV}d}, i_{{\rm HV}q}\}$ are the dq components of the HV-side grid voltage and current, respectively, where second-order-generalized integrators have been used [22]. The modulation signal for the jth H-bridge submodule, $m_{I,j}$ in Fig. 2, is then calculated by dividing the α component of the current control output by N-times the corresponding dc-link capacitor voltage, $v_{I,j}$.

(b) Stage-II control: For this stage, the control design aims at (i) regulating the LV-side dc-link capacitor energy to the prescribed reference e_{II}^*, while (ii) evenly distributing the sum of energy in the HV capacitors. This is achieved via N PI control loops. Specifically, (i) is achieved by a common PI loop for the N DABs [denoted as $G_{II,e}(s)$ in Fig. 2], which provides a common power reference $p_{\rm II}^*$, while (ii) is achieved by $N-1$ individual PI loops for each DAB [denoted as $G_{{\rm II},pb}(s)$ in Fig. 2], which provide individual incremental power terms $\Delta p_{{\rm II},j}$, which satisfy $\Sigma_{j=1}^{N} \Delta p_{{\rm II},j} = 0$. To account for nonlinearities of DAB and facilitate current sharing among input-series output-parallel modules, inner current controllers are employed using individual PI controller for each DAB [denoted as $G_{{\rm II},i}(s)$ in Fig. 2], which provide the required phase-shift, ϕ_j for individual DAB modules [2], [23].

(c) Stage-III control: With PI controller $G_{{\rm III},i}(s)$ in Fig. 2, Stage III uses a similar current control loop as Stage I to steer the LV-side active and reactive powers, $p_{\rm III}$ and $q_{\rm III}$, to their prescribed reference values, $p_{\rm III}^*$ and $q_{\rm III}^*$. Similar to (5), $v_{{\rm LV}d,ff}$ and $v_{{\rm LV}q,ff}$ are the decoupling feedforward terms. The control laws of the outer control loops are summarized in Table I.

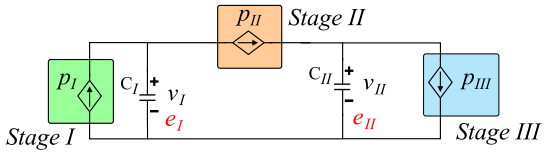

Fig. 3. Averaged-model of a single-phase single-string SST.

2) DC: Mao et al. [15] proposed a change in state variables, such that the Stage I controls the sum of total dc-link energies e_Σ with an aim to decouple the power flow in Stage I from Stage II.

3) BC: Sarda et al. [17] proposed a new set of variables with coupled load transient ability, such that Stage I controls the sum of total dc-link energies e_Σ, as in [15], while Stage II controls the difference in energies $e_{\rm II} - e_{{\rm I},j}$.

4) Summary: A brief summary of the state variables and corresponding control laws used in the different control strategies are summarized in Table I. The incremental states in Table I is denoted as $\tilde{y}$ and defined with respect to the equilibrium pointy^* as$\tilde{y} = y - y^*$.Pair $\{\alpha_1, \alpha_2\}$ in Table I represents the PI gains for Stage-I outer energy controller [$G_{{\rm I},e}(s)$ in Fig. 2] and, similarly, $\{\beta_1, \beta_2\}$ and $\{\xi_1, \xi_2\}$ pairs represent the PI gains for Stage-II energy controller [$G_{{\rm II},e}(s)$] and power balancing controller [$G_{{\rm II},pb}(s)$], respectively. During any transient event, the dc-link capacitors $C_{{\rm I},j}$ and $C_{\rm II}$ compensate for disturbances, resulting in corresponding energy variations represented as $\tilde{e}_{{\rm I},j}$ and $\tilde{e}_{\rm II}$. It is important to recognize that an appropriate energy distribution within the capacitors is essential for the system's reliable operation, which is discussed next. The inner current loops [$G_{{\rm I},i}(s)$, $G_{{\rm II},i}(s)$ and $G_{{\rm III},i}(s)$] are designed at a faster dynamics than the outer loops, which explanation is avoided for the sake of brevity [13].

III. ENERGY DISTRIBUTION IN DC-LINK CAPACITORS DURING LOAD TRANSIENT

The single-string averaged model of the SST shown in Fig. 3 [17] is considered for the analysis in this section. In Fig. 3, $p_{\rm I}$, $p_{\rm II}$, and $p_{\rm III}$ represent the averaged powers over a grid frequency, through Stages I, II, and III, respectively. The dynamic model

of the system in Fig. 3 corresponds to

$$\dot{e}_I = p_{\rm I} - p_{\rm II} \tag{6}$$

$$\dot{e}_{II} = p_{\rm II} - p_{\rm III} \tag{7}$$

or, equivalently, in terms of incremental variables

$$\dot{\tilde{e}}_{\rm I} = \tilde{p}_{\rm I} - \tilde{p}_{\rm II} \tag{8}$$

$$\dot{\tilde{e}}_{\rm II} = \tilde{p}_{\rm II} - \tilde{p}_{\rm III} \tag{9}$$

1) CC: Replacing $\tilde{p}_{\rm I}$ and $\tilde{p}_{\rm II}$ in (8) and (9) by the control laws given in the first column of Table I, the following closed-loop state-space representation is obtained

$$\dot{\tilde{x}} = \begin{bmatrix} -\alpha_1 & \beta_1 & -\alpha_2 & \beta_2 \\ 0 & -\beta_1 & 0 & -\beta_2 \\ 1 & 0 & 0 & 0 \\ 0 & 1 & 0 & 0 \end{bmatrix} \tilde{x} + \begin{bmatrix} 0 \\ -1 \\ 0 \\ 0 \end{bmatrix} \tilde{p}_{\rm III}. \tag{10}$$

$\tilde{x} = [\tilde{e}_{\rm I} \tilde{e}_{\rm II} \ \int \tilde{e}_{\rm I} \ \int \tilde{e}_{\rm II}]'$ denotes the state vector, where integral variables have been considered to enforce zero steady-state error in the regulation of $e_{\rm I}$ and $e_{\rm II}$ regardless of the unknown load. From (10), the following energy-to-load transfer functions can be obtained:

$$\frac{\tilde{E}_{\rm I}(s)}{\tilde{P}_{\rm III}(s)} = -\frac{\beta_1 + \frac{\beta_2}{s}}{(s + \alpha_1 + \frac{\alpha_2}{s})(s + \beta_1 + \frac{\beta_2}{s})} \tag{11}$$

$$\frac{\tilde{E}_{\rm II}(s)}{\tilde{P}_{\rm III}(s)} = -\frac{1}{s + \beta_1 + \frac{\beta_2}{s}}. \tag{12}$$

Adding (11) and (12), the total energy-to-load transfer function is obtained as

$$\frac{\tilde{E}_{\Sigma}(s)}{\tilde{P}_{\rm III}(s)} = -\frac{1}{s + \alpha_1 + \frac{\alpha_2}{s}} \left(\frac{\alpha_1 + \frac{\alpha_2}{s}}{s + \beta_1 + \frac{\beta_2}{s}} + 1 \right). \tag{13}$$

Dividing (11) by (12), the following energy-to-energy transfer function is obtained:

$$\frac{\tilde{E}_{\rm I}(s)}{\tilde{E}_{\rm II}(s)} = \frac{\beta_1 + \frac{\beta_2}{s}}{s + \alpha_1 + \frac{\alpha_2}{s}}. \tag{14}$$

The transfer function (13) provides information about how the total (or global) energy stored in the SST changes according to a load change, whereas (14) defines how the energy within the SST distributes internally. As it can be observed, the control parameters of both Stage I and II, i.e., pairs $\{\alpha_1, \alpha_2\}$ and $\{\beta_1, \beta_2\}$, affect the transfer functions (13) and (14), challenging the control design. For the sake of simplicity, a ratio k is defined between Stage-II and Stage-I feedback gains, i.e.,

$$\beta_i = k\alpha_i, \forall i \in \{1, 2\}. \tag{15}$$

Further examining (13) and (14), the following time-domain responses to a unit-step change in the load are obtained:

$$\tilde{e}_{\Sigma}(t) \approx \frac{1}{\alpha_1} \left(\frac{1}{k} + 1 \right) e^{-\frac{\alpha_2}{\alpha_1} t} \tag{16}$$

$$\tilde{e}_{\rm I}(t) \approx k\tilde{e}_{\rm II}(t). \tag{17}$$

The first-order approximations in (16) and (17) is valid under dominant-pole condition $\alpha_1^2 >> 4\alpha_2$. From (16) and (17), the following conclusions can be drawn:

1) From (16), if $k > 10$, the peak energy change in $\tilde{e}_{\Sigma}$ (denoted as $\tilde{e}_{\Sigma-p}$) remains equivalent to approximately $\frac{1}{\alpha_1}$. However, $\tilde{e}_{\Sigma-p}$ increases as the gain ratio k decreases when below 10. Therefore, $k < 10$ is undesired in the CC.
2) From (17), the individual peak energy changes in $C_{\rm I}$ and $C_{\rm II}$ (denoted as $\tilde{e}_{{\rm I}-p}$ and $\tilde{e}_{{\rm II}-p}$) follows $\tilde{e}_{{\rm I}-p} > \tilde{e}_{{\rm II}-p}$ $\forall t$ when $k > 1$, indicating a greater reliance on the energy stored in the HV-side capacitors to compensate for load transients.

To validate the preceding conclusions, simulations are performed on the reduced-order model depicted in Fig. 3, assessing its response to a unit step change in load power, $p_{\rm III}$, for different k values, viz., $k \in \{1, 5, 10, 20, 50, 100\}$. The Stage-I control gains are chosen as $\alpha_1 = 50$ and $\alpha_2 = 100$, ensuring $\alpha_1^2 >> 4\alpha_2$ and an adequate rise time of less than 40 ms. The peak values in the incremental energy variables $\tilde{e}_{\Sigma-p}$, $\tilde{e}_{{\rm I}-p}$, and $\tilde{e}_{{\rm II}-p}$ are recorded and compared with the theoretical values derived in (17) and (18), and shown in Fig. 4(a). For example, with $k = 100$, $\tilde{e}_{\Sigma-p}$, $\tilde{e}_{{\rm I}-p}$, and $\tilde{e}_{{\rm II}-p}$ are 0.018 J, 0.018 J, and 0.00018 J. The maximum energy variation in $\tilde{e}_{\Sigma}$ approximately matches the $1/\alpha_1 = 0.02$ value indicated in conclusion 1) for $k > 10$. Besides, the ratio $\tilde{e}_{{\rm I}-p}/\tilde{e}_{{\rm II}-p}$ matches the $k = 100$ value indicated in conclusion 2).

On the other hand, for $k = 1$, $\tilde{e}_{\Sigma-p}$, $\tilde{e}_{{\rm I}-p}$, and $\tilde{e}_{{\rm II}-p}$ are 0.036J, 0.018J, and 0.018J, respectively. The maximum energy variation in $\tilde{e}_{\Sigma}$ approximately matches the $1/\alpha_1(1/k + 1) \approx 0.036$ value indicated in conclusion 1) for $k < 10$. Besides, the ratio $\tilde{e}_{{\rm I}-p}/\tilde{e}_{{\rm II}-p}$ matches the $k = 1$ value indicated in conclusion 2). Minor discrepancies can be attributed to the neglected effect of the integral terms.

2) DC: The analysis performed in this section follows the same methodology as outlined in the previous section; therefore, it is not reiterated here. The main results are summarized in the second column of Table II, followed by the next concluding remarks.

1) Unlike the CC, the peak energy change $\tilde{e}_{\Sigma-p}$ remains equivalent to approximately $\frac{1}{\alpha_1}$, irrespective of k.
2) Owing to conclusion 1), the individual peak energy changes $\tilde{e}_{{\rm I}-p}$ and $\tilde{e}_{{\rm II}-p}$ obtained are $(1 - \frac{1}{k})\tilde{e}_{\Sigma-p}$ and $\frac{1}{k}\tilde{e}_{\Sigma-p}$, respectively, showing that the distribution can be adjusted by selecting different values of k, without impacting the global peak energy change $\tilde{e}_{\Sigma-p}$.

Similar simulation results to those in the previous section are conducted. These results are illustrated in Fig. 4(b), clearly matching the predicted values and corroborating the preceding conclusions. Notably, $\tilde{e}_{\Sigma-p}$ (red curve) is constant throughout the simulation, and approximately equal to the $1/\alpha_1 = 0.02$ value regardless the k value. The individual peak energy distribution $\tilde{e}_{{\rm I}-p} - \tilde{e}_{{\rm II}-p}$ (blue curve) can be adjusted according to the value of k without impacting $\tilde{e}_{\Sigma-p}$, which stands apart from the CC. For example, by choosing $k = 1$, the $\tilde{e}_{{\rm I}-p} \approx 0$J and $\tilde{e}_{{\rm II}-p} \approx 0.02$J, relaxing the transient energy compensation from $C_{\rm I}$. Conversely, by choosing $k > 10$, the $\tilde{e}_{{\rm I}-p} \approx 0.02$J and $\tilde{e}_{{\rm II}-p} \approx 0$J, relaxing the transient energy compensation from $C_{\rm II}$.

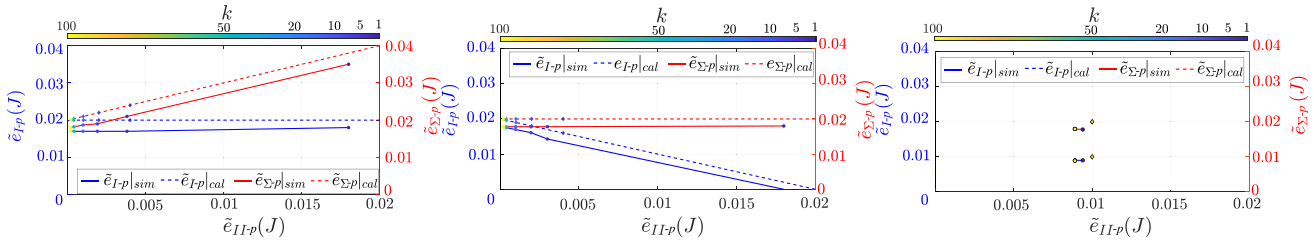

Fig. 4. SST global energy variation (peak value) ($\tilde{e}_{\Sigma-p}$) and internal distribution charts ($\tilde{e}_{\mathrm{I}-p}$ and $\tilde{e}_{\mathrm{II}-p}$), where $\{\tilde{e}_{\Sigma-p|\mathrm{sim}}\tilde{e}_{I-p|\mathrm{sim}}\}$ are the simulated values and $\{\tilde{e}_{\Sigma-p|\mathrm{cal}}\tilde{e}_{I-p|\mathrm{cal}}\}$ are the calculated values from Table I, for: (a) CC, (b) DC, and (c) BC.

TABLE II
COMPARISON OF TOTAL INCREMENTAL ENERGY DISTURBANCE AND RATIO OF INCREMENTAL ENERGY DISTRIBUTION AMONG C_{I} AND C_{II}

Comparison Metric	Conventional Control [13]	Decoupled Control [15]	Balanced Control [17]
Energy charts	Fig. 4(a)	Fig. 4(b)	Fig. 4(c)
Closed-loop state matrix	$\begin{bmatrix} -\alpha_1 & \beta_1 & -\alpha_2 & \beta_2 \\ 0 & -\beta_1 & 0 & -\beta_2 \\ 1 & 0 & 0 & 0 \\ 0 & 1 & 0 & 0 \end{bmatrix}$	$\begin{bmatrix} -\alpha_1 & \beta_1-\alpha_1 & -\alpha_2 & \beta_2-\alpha_2 \\ 0 & -\beta_1 & 0 & -\beta_2 \\ 1 & 0 & 0 & 0 \\ 0 & 1 & 0 & 0 \end{bmatrix}$	$\begin{bmatrix} -\beta_1 & \beta_1 & -\beta_2 & \beta_2 \\ \beta_1-\alpha_1 & -\alpha_1-\beta_1 & \beta_2-\alpha_2 & -\alpha_2-\beta_2 \\ 1 & 0 & 0 & 0 \\ 0 & 1 & 0 & 0 \end{bmatrix}$
Closed-loop eigenvalues	$\frac{1}{2}\begin{bmatrix} -\alpha_1-\sqrt{\alpha_1^2-4\alpha_2} \\ \sqrt{\alpha_1^2-4\alpha_2}-\alpha_1 \\ -\beta_1-\sqrt{\beta_1^2-4\beta_2} \\ \sqrt{\beta_1^2-4\beta_2}-\beta_1 \end{bmatrix}$	$\frac{1}{2}\begin{bmatrix} -\alpha_1-\sqrt{\alpha_1^2-4\alpha_2} \\ \sqrt{\alpha_1^2-4\alpha_2}-\alpha_1 \\ -\beta_1-\sqrt{\beta_1^2-4\beta_2} \\ \sqrt{\beta_1^2-4\beta_2}-\beta_1 \end{bmatrix}$	$\frac{1}{2}\begin{bmatrix} 2\sqrt{\beta_1^2-2\beta_2}-2\beta_1 \\ -\alpha_1-\sqrt{\alpha_1^2-4\alpha_2} \\ \sqrt{\alpha_1^2-4\alpha_2}-\alpha_1 \\ -2\beta_1-2\sqrt{\beta_1^2-2\beta_2} \end{bmatrix}$
Stability criteria	$\alpha_1,\alpha_2,\beta_1,\beta_2>0$	$\alpha_1,\alpha_2,\beta_1,\beta_2>0$	$\alpha_1,\alpha_2,\beta_1,\beta_2>0$
$\frac{\tilde{E}_\Sigma(s)}{\tilde{P}_{III}(s)}$	$-\frac{1}{s+\alpha_1+\frac{\alpha_2}{s}}\left(\frac{\alpha_1+\frac{\alpha_2}{s}}{s+\beta_1+\frac{\beta_2}{s}}+1\right)$	$-\frac{1}{(s+\alpha_1+\frac{\alpha_2}{s})}$	$-\frac{1}{(s+\alpha_1+\frac{\alpha_2}{s})}$
$\frac{\tilde{E}_I(s)}{\tilde{E}_{II}(s)}$	$\frac{\beta_1+\frac{\beta_2}{s}}{s+\alpha_1+\frac{\alpha_2}{s}}$	$\frac{\beta_1-\alpha_1+\frac{\beta_2-\alpha_2}{s}}{s+\alpha_1+\frac{\alpha_2}{s}}$	$\frac{\beta_1+\frac{\beta_2}{s}}{s+\beta_1+\frac{\beta_2}{s}}$
$\tilde{e}_I(t)$ for unit step change in $\tilde{p}_{III}$	$\frac{1}{\alpha_1}e^{-\frac{\alpha_2}{\alpha_1}t}$	$\frac{1}{\alpha_1}(1-\frac{1}{k})e^{-\frac{\alpha_2}{\alpha_1}t}$	$\frac{1}{2\alpha_1}e^{-\frac{\alpha_2}{\alpha_1}t}$
$\tilde{e}_{II}(t)$ for unit step change in $\tilde{p}_{III}$	$\frac{1}{\alpha_1 k}e^{-\frac{\alpha_2}{\alpha_1}t}$	$\frac{1}{\alpha_1 k}e^{-\frac{\alpha_2}{\alpha_1}t}$	$\frac{1}{2\alpha_1}e^{-\frac{\alpha_2}{\alpha_1}t}$
$\tilde{e}_\Sigma(t)$ for unit step change in $\tilde{p}_{III}$	$\frac{1}{\alpha_1}(\frac{1}{k}+1)e^{-\frac{\alpha_2}{\alpha_1}t}$ increases as k decreases	$\frac{1}{\alpha_1}e^{-\frac{\alpha_2}{\alpha_1}t}$ invariant on k	$\frac{1}{\alpha_1}e^{-\frac{\alpha_2}{\alpha_1}t}$ invariant on k
Energy distribution	$\tilde{e}_I\approx k\tilde{e}_{II}$ $\tilde{e}_I>\tilde{e}_{II}\ \forall k>1$ partially controllable with k	$\tilde{e}_I\approx(k-1)\tilde{e}_{II}$ linear distribution fully controllable with k	$\tilde{e}_I\approx\tilde{e}_{II}$ uncontrollable with k

This property of the DC will be used to improve the operational stability of the SST to withstand higher load transients, discussed in Section IV.

3) BC: The main results are summarized in the third column of Table II, followed by the next concluding remarks.

1) Similar to the DC, the peak energy change $\tilde{e}_{\Sigma-p}$ remains equivalent to approximately $\frac{1}{\alpha_1}$, irrespective of k.
2) Unlike the DC, the distribution of peak energies among C_{I} and C_{II} is always equal irrespective of k, i.e., $\tilde{e}_{\mathrm{I}-p}\approx\tilde{e}_{\mathrm{II}-p}\approx\frac{1}{2}\tilde{e}_{\Sigma-p}$.

Fig. 4(c) corroborates the accuracy of the analysis via simulations. Notably, $\tilde{e}_{\Sigma-p}$ (red curve) is constant throughout the simulation, and approximately equal to the $1/\alpha_1=0.02$ value regardless the k value. However, the individual peak energy distribution $\tilde{e}_{\mathrm{I}-p}-\tilde{e}_{\mathrm{II}-p}$ (blue curve) cannot be adjusted according to the value of k, which stands apart from the DC. For example, choosing $k=1$ or $k=10$ results in $\tilde{e}_{\mathrm{I}-p}\approx 0.01$J and $\tilde{e}_{\mathrm{II}-p}\approx 0.01$J, making the distribution independent of k.

4) Remarks: Note that all the above-discussed controls yield theoretically stable closed-loop systems (with closed-loop state matrix being Hurwitz) as long as the feedback gains are non-negative. However, to ensure operational stability and prevent unsafe or nonlinear operation that could lead to instability, it is crucial that the state variables, e_{I} and e_{II}, remain within a specified constrained region. For instance, e_I must be larger than the peak value of the HV-side grid voltage to prevent

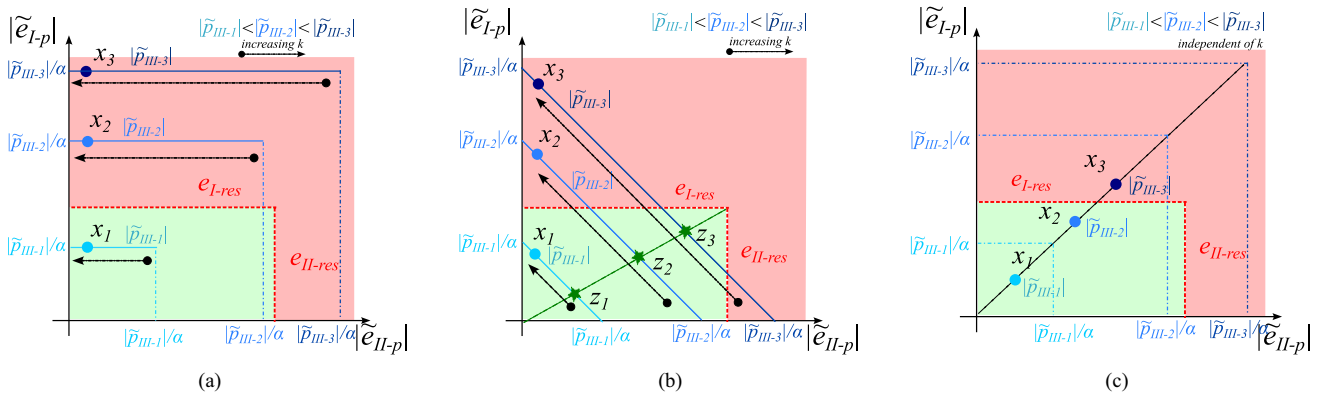

Fig. 5. SST global energy variation and internal distribution charts illustrating reserved energies under different load conditions, with operating points $\{x_1, x_2, x_3\}$ depicting the particular $k = 10$ case. (a) CC, (b) DC, and (c) BC. Operating points $\{z_1, z_2, z_3\}$ in (b) depict the optimal k values that maximise the SST operating region.

overmodulation yet lower than a prescribed maximum value to prevent unsafe operation. Note that, the generalization of the results for an N-string SST is provided in an Appendix. The next section defines the viable operational regions and evaluates the suitability of the previously discussed control strategies to maintain operation within them.

IV. Reserve-Energy-Aided Control Design Approach

In this section, the concept of energy reserve is used to assess the operational stability of the SST. Energy reserve refer to the amount of energy that a capacitor can absorb or supply without exceeding operational limits beyond which SST stability (or safety) may be compromised. For example, for the sum of energies in the HV-side capacitors, e_I, its energy reserve is given by

$$e_{\text{I-res}} = \begin{cases} e_{\text{I}}^* - \frac{1}{2} C_{\text{I}} V_{\text{I-min}}^2 & \forall \tilde{e}_{\text{I}} < 0 \\ \frac{1}{2} C_{\text{I}} V_{\text{I-max}}^2 - e_{\text{I}}^* & \forall \tilde{e}_{\text{I}} > 0 \end{cases} \tag{18}$$

where $V_{\text{I-max}}$ and $V_{\text{I-min}}$ are the maximum and minimum voltage levels of operation for C_{I}, respectively. Note that, the choice of $V_{\text{I-max}}$ is defined by the switch and capacitor voltage ratings, and $V_{\text{I-min}}$ is defined by the CHB ac-side voltage reference to avoid overmodulation. Similarly, defining $V_{\text{II-max}}$ and $V_{\text{II-min}}$ as the maximum and minimum voltage levels of operation for C_{II}, the reserve energy is obtained as $e_{\text{II-res}}$ similar to (18).

Fig. 5 depicts the operating ranges of the SST on the $|\tilde{e}_{\text{I}-p}| - |\tilde{e}_{\text{II}-p}|$ plane, with safe regions highlighted in green and unsafe regions in red. The safe operating range is defined by the conditions $|\tilde{e}_{\text{I}-p}| < e_{\text{I-res}}$ and $|\tilde{e}_{\text{II}-p}| < e_{\text{II-res}}$, while the unsafe range is where $|\tilde{e}_{\text{I}-p}| > e_{\text{I-res}}$ or $|\tilde{e}_{\text{II}-p}| > e_{\text{II-res}}$. Red dashed lines illustrate the limits between safe and unsafe regions. The figure compares the CC [see Fig. 5(a)], the DC [see Fig. 5(b)], and the BC [see Fig. 5(c)]. These comparisons are made under three different load changes denoted as $|\tilde{p}_{\text{III}-1}|$, $|\tilde{p}_{\text{III}-2}|$, and $|\tilde{p}_{\text{III}-3}|$, where $|\tilde{p}_{\text{III}-1}| < |\tilde{p}_{\text{III}-2}| < |\tilde{p}_{\text{III}-3}|$. The SST global energy variation charts illustrated in Fig. 4 are superimposed in the $|\tilde{e}_{\text{I}-p}| - |\tilde{e}_{\text{II}-p}|$ plane of Fig. 5 for the three different load changes, where marker points x_1, x_2, x_3 highlight the corresponding operating points for the particular $k = 10$ case. Note that different k values will correspond to different points along the lines for the CC and the DC, whereas it will remain unchanged for the BC.

Note that as the load change increases in magnitude, the operating points x_1, x_2, x_3 tend to move toward the unsafe region regardless the control strategy adopted. Nevertheless, it is important to highlight that, unlike the CC and the BC, the DC can remain within the safe area of operation for a given range of k values for the three different load changes considered. For instance, if the k values in the DC are chosen such that $\{x_1, x_2, x_3\}$ become $\{z_1, z_2, z_3\}$, highlighted with star markers in Fig. 5(b), the SST will maximize its operation within the safe region. Note that $\{z_1, z_2, z_3\}$ correspond to the intersection between the line $|\tilde{e}_{\text{I}-p}| = e_{\text{I-res}}/e_{\text{II-res}} * |\tilde{e}_{\text{II}-p}|$ [green-dashed line in Fig. 5(b)] and load-dependent line $|\tilde{e}_{\text{I}-p}| + |\tilde{e}_{\text{II}-p}| = |\tilde{e}_{\Sigma-p}| \approx |\tilde{p}_{\text{III}}|/\alpha_1$, where $|\tilde{e}_{I-p}| = (k-1)|\tilde{e}_{\text{II}-p}|$. Equating the line equations, the optimal k value can be found as

$$k = 1 + \frac{e_{\text{I-res}}}{e_{\text{II-res}}} \tag{19}$$

which provides an efficient way of distributing energies and utilizing reserved energy to allow maximum load change without hitting converter limits, ensuring operational stability. Next section presents experimental verification of the results obtained in Section III and this section.

A. Remarks

1) Influence of Stage-I Control Gain (α_1): Fig. 5 depicts feasible energy distributions for different load cases ($\tilde{p}_{\text{III}-1} < \tilde{p}_{\text{III}-2} < \tilde{p}_{\text{III}-3}$), keeping the control gains of Stage I constant. Note that this is a valid assumption since, in practice, the Stage I control gains are determined to ensure accurate control of the HV-side grid current, as described in Section IV-A. Having said this, it is worth mentioning that the proposed theoretical framework is sufficiently general to consider variations in both the load and the Stage-I control gain.

2) Minimum Energy Reserve Requirement: Note that the energy reserve values, or equivalently the capacitance and dc values of the capacitor voltages, should not be too restrictive. In fact, for a transient to be feasible, the HV and LV peak energy

TABLE III
MAXIMUM LOAD CHANGE USING DIFFERENT CONTROL STRATEGIES

	Conventional Control	Decoupled Control	Balanced Control	Proposed Control
$\tilde{p}_{III-max}$	$\min(\alpha_1 e_{I-res}, \beta_1 e_{II-res})$	$\min(\frac{\alpha_1\beta_1}{\beta_1-\alpha_1} e_{I-res}, \beta_1 e_{II-res})$	$\min(2\alpha_1 e_{I-res}, 2\alpha_1 e_{II-res})$	$\alpha_1(e_{I-res}+e_{II-res})$

transients must satisfy the following conditions:

$$\tilde{e}_{\mathrm{I}-p} \leq e_{\mathrm{I-res}} \tag{20}$$

$$\tilde{e}_{\mathrm{II}-p} \leq e_{\mathrm{II-res}} \tag{21}$$

beyond which the prescribed fault limits are inevitable. Using the maximum values obtained for $\tilde{e}_{\mathrm{I}-p}$ and $\tilde{e}_{\mathrm{II}-p}$ from Table II for each of the studied control strategies, the maximum load change, denoted as $\tilde{p}_{\mathrm{III-max}}$, preserving the linear region of operation, is given in Table III.

From Table III, it can be observed that the maximum load change capability for the proposed control is determined by both $e_{\mathrm{I-res}}$ and $e_{\mathrm{II-res}}$ simultaneously, unlike the other controls where $\tilde{p}_{\mathrm{III-max}}$ is limited either by $e_{\mathrm{I-res}}$ or $e_{\mathrm{II-res}}$. The inequalities presented in Table III can serve as a guideline for appropriately sizing the HV and LV dc-link capacitors to handle a desired range of load changes. Alternatively, for a given set of capacitance values selected based on voltage ripple criteria, the inequalities in Table III can be used to determine the load range capability of the SST.

3) Effect of Capacitance Degradation: The bandwidth ratio proposed in (19) is influenced by capacitance variations. For the experimental setup detailed in Section V, a $\pm 20\%$ variation in C_{I} and C_{II} results in an approximately $\pm 10\%$ fluctuation in the optimal k. However, this variation is mild and can be effectively mitigated through the use of online capacitance monitoring methods [24], [25], allowing for dynamic adjustment of the relative gain k.

V. EXPERIMENTAL RESULTS

To validate the analysis in Section III and the proposed reserve-energy-aided control design approach in Section IV, a small-scale laboratory prototype is built, as shown in Fig. 6, with parameters listed in Table III. It comprises of two strings, with Stage I connected to a GE & EL 15-kVA CINERGIA grid emulator, and with Stage III emulated by a Chroma 63200E electronic load. The control system is implemented using Imperix B-Box RCP at a sampling frequency of 20 kHz. The six H-bridges (three per string) are implemented using Infineon SiC IMZ120R045M1 devices. The DAB implementation makes use of a five-stacked E70 ferrite core transformer with 9 turns on both the primary and secondary sides operating at 50 kHz. The conventional phase-shifted sinusoidal pulsewidth modulation technique is used for the CHB, and single phase shift modulation strategy is used for the DABs. The Imperix B-Box RCP collects sensor data via analog-to-digital conversion channels, and MATLAB is utilized for postprocessing and plotting the waveforms.

In this section, the energy distribution plots in Fig. 4 are compared against experimental results to experimentally corroborate the accuracy of the proposed analysis. Subsequently, the concept of operational instability is demonstrated with the conventional, the decoupled, and the balanced controllers for different load changes. Finally, the improved results with redesigned control gain based on the reserve-energy concept using (19) is presented. Stage-I control parameters $\{\alpha_1, \alpha_2\}$ are chosen as {50, 100} to ensure a phase margin greater than 60° and bandwidth less than $1/5$th of the grid frequency (50 Hz).

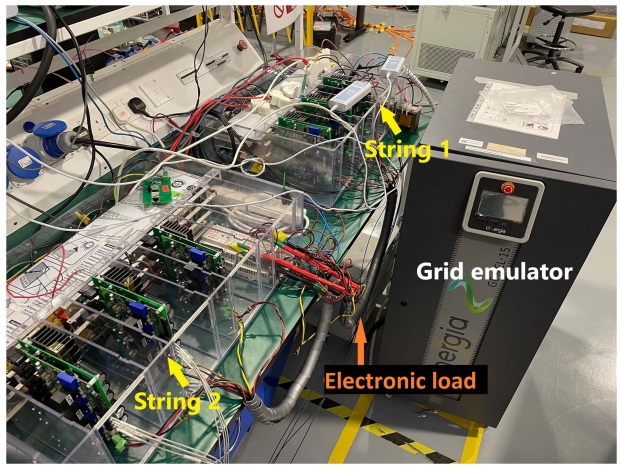

Fig. 6. Experimental setup of a 1-kVA 230-V/250-V, 50-kHz SST.

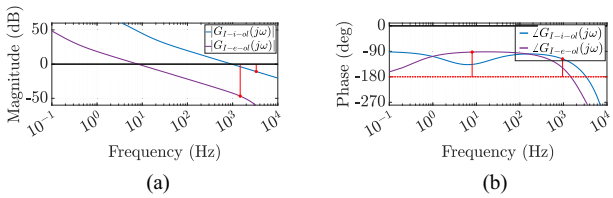

(a) (b)

Fig. 7. Open-loop Bode plots of the inner current control loop and outer energy control loop of Stage I (a) magnitude and (b) phase.

A. Selection of Stages-I and II Control Gains

The PI gains of the inner current control loop are chosen to achieve a bandwidth of 1 kHz (more than 10-times lower than the CHB equivalent switching frequency) and a phase margin of 60°. Specifically, $\gamma_1 = 120$ and $\gamma_2 = 12000$.

With respect to the PI gains of the outer energy control loop, a bandwidth of 10 Hz (one fifth of the grid fundamental frequency) and a phase margin of 90° have been considered. Specifically, $\alpha_1 = 50$ and $\alpha_2 = 100$. The corresponding open-loop Bode plots are given in Fig. 7(a) and (b). Note that the chosen values for the control parameters of Stage I are unchanged for all the studied controllers in the following experiments.

For Stage-II control, a relative bandwidth of $k = 10$ is selected for the CC, DC, and BC, while k is determined based on (19) for the proposed control. The choice of $k \geq 10$ adheres to the

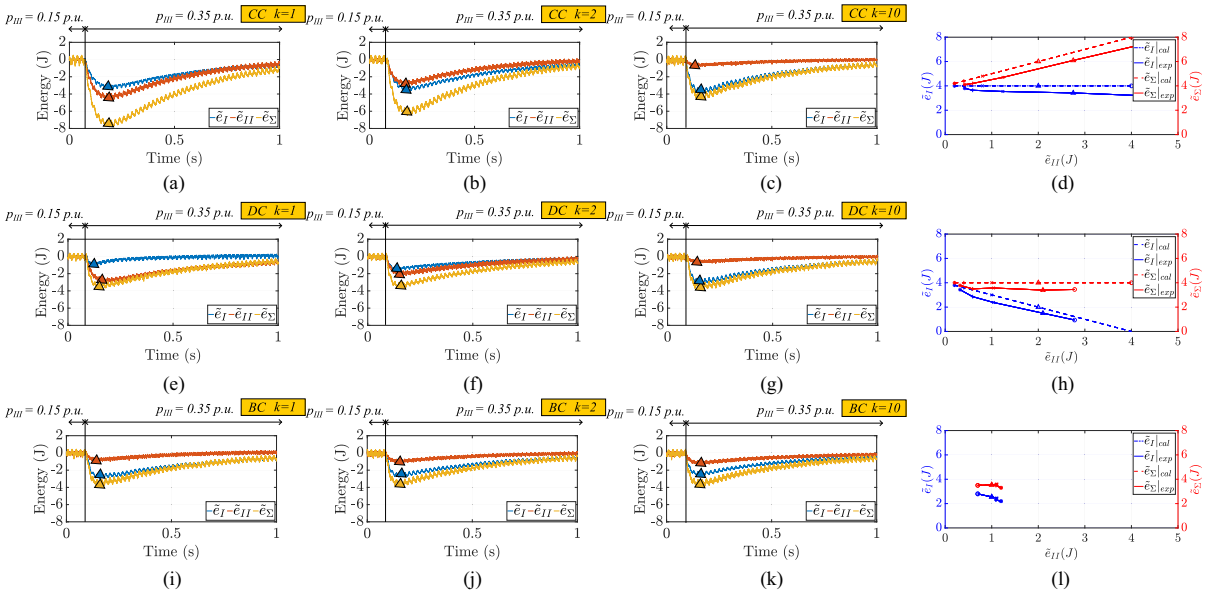

Fig. 8. Experimental SST global energy variation and internal distribution charts ($\tilde{e}_I$, $\tilde{e}_{\text{II}}$ and $\tilde{e}_\Sigma$) for a step load change from 0.15 to 0.35 p.u with different values of k(1, 2, 10, 20). From left to right, time-domain energy variations with (left column) $k = 1$, (middle-left column) $k = 2$, (middle-right column) $k = 10$, and (right column) energy distribution chart using different controls. From top to bottom, (a)–(d) CC, (e)–(h) DC, and (i)–(l) BC.

conventional design approach in the literature [13], [15], which recommends maximizing the control bandwidth of individual SST stages.

B. Experimental Verification of the Global Energy Variation and Internal Distribution Charts

On the experimental test bench depicted in Fig. 6, a step change in load from 0.15 p.u to 0.35 p.u is performed and the peak energy variations in the incremental energy variables $\tilde{e}_{I-p}$, $\tilde{e}_{II-p}$ and $\tilde{e}_{\Sigma-p}$ are recorded and shown in Fig. 8. From top to bottom, Fig. 8 displays the energy distribution using CC in Fig. 8(a)–(d), DC in Fig. 8(e)–(h), and BC in Fig. 8(i)–(l). Fig. 8 shows the effect of different k values $\{1, 2, 10\}$. The highlighted maximum changes in energy in Fig. 8(a)–(c) are used to plot Fig. 8(d), which show agreement with the results obtained using reduced-order model in Fig. 4(a). Similarly, Fig. 8(h) and (l) for decoupled and BC show agreement with the results obtained in Fig. 4(b) and (c), respectively.

As discussed in Section II, using the CC, and high values of k reported in existing literature ($k > 10$), $\tilde{e}_{\Sigma-p}$ can be kept relatively constant in the detriment of an increased burden on the HV dc-link capacitors, i.e., $\tilde{e}_{\text{I}-p} > \tilde{e}_{\text{II}-p}$. Although k can be reduced to $k < 10$ values for a fairer distribution of energies between HV and LV dc-link capacitors, an undesirable increase in $\tilde{e}_\Sigma$ is observed, as Fig. 8(a)–(d) corroborate. Specifically, in Fig. 8(a), $\tilde{e}_{\text{I}-p}$ and $\tilde{e}_{\text{II}-p}$ are relatively close, but $\tilde{e}_{\Sigma-p}$ is approximately twice larger (in absolute value) than in Fig. 8(c).

Using the DC, a linear distribution of energies among C_{I} and C_{II} can be achieved with a suitable choice of k as seen in Fig. 8(e)–(h). Remarkably, $\tilde{e}_{\Sigma-p}$ remains constant irrespective of the k value. For $k = 1$ in Fig. 8(e), the LV dc-link capacitor is responsible of providing approximately all the required transient energy, whereas, as k increases, the roles shift in a linear fashion to the point that at $k = 10$, in Fig. 8(h), the HV dc-link capacitors are the ones responsible of providing almost all the transient energy. In fact, this is the underlying basis of the proposed control design approach, where the value of k is adjusted according to (19) to optimally distribute the energy transient.

In Fig. 8(i)–(l), the distribution of energies using BC is presented. Irrespective of k, the energy among $C_{\text{I},j}$ and C_{II} are distributed evenly, i.e., $\tilde{e}_{\text{I},1-p} \approx \tilde{e}_{\text{I},2-p} \approx \tilde{e}_{\text{II}-p}$ (or equivalently, $\frac{1}{N}\tilde{e}_{\text{I}-p} \approx \tilde{e}_{\text{II}-p}$) with $\tilde{e}_{\Sigma-p}$ remaining constant, resembling equivalency of the results obtained using reduced-order model in Fig. 4(c).

Note that, unlike the equivalent single-string reduced-order model used to obtain Fig. 4, the results obtained are for $N = 2$ strings and 200-W step change in load power, representing a 200-time scaled-up version. However, the conclusions remain valid.

The authors acknowledge slight discrepancies between the calculated and the experimental results. The discrepancies arise from simplifications in the theoretical derivations, including neglecting integral terms, disregarding second harmonics on HV-side capacitors, and omitting nonlinear effects like dead time in DAB converters.

C. Operational Instability Mechanism of CC Approaches

This section compares the performance of the proposed reserved-energy-aided control design approach, where k is chosen according to (19), against the studied controllers in this article for $k = 10$ value. Two load changes are used to illustrate the operational instability mechanism of the CC approaches: a 0.5 p.u increase in power and a 0.7 p.u decrease in power, as shown in Figs. 9 and 10, respectively. The DC with the proposed design approach is then tested for the same load changes as

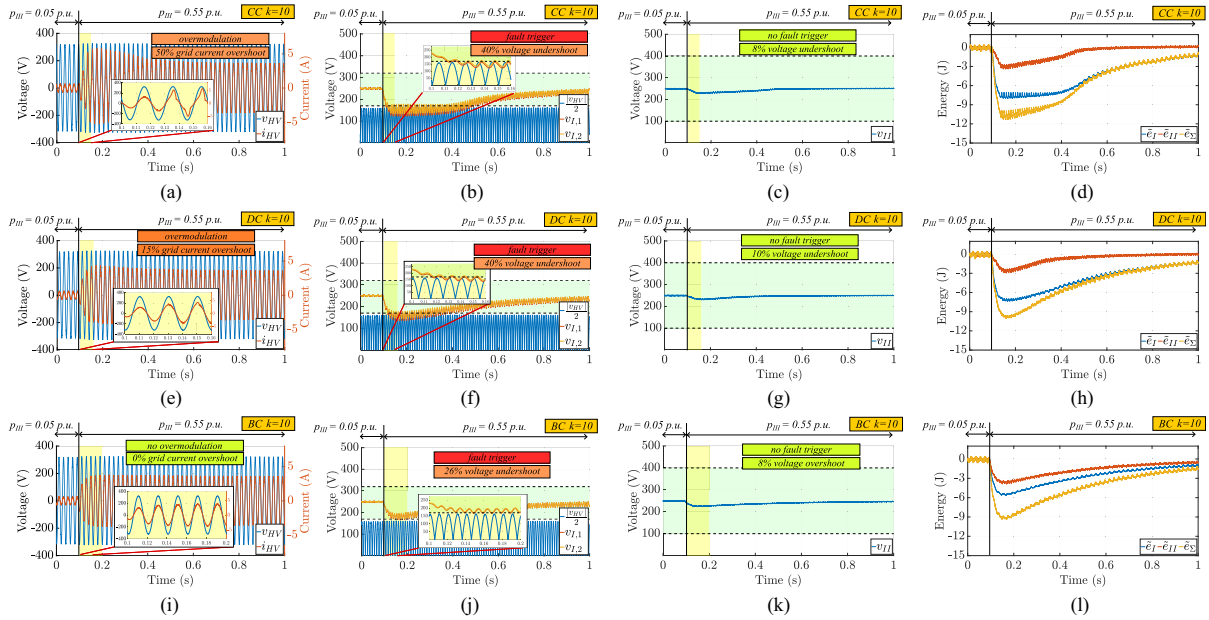

Fig. 9. Experimental results for a step load change from 0.05 to 0.55 p.u From left to right, (left column) HV grid voltage (v_{HV}) and HV grid current (i_{HV}) (middle-left column) HV DC-link capacitor voltages ($v_{\mathrm{I},1}$ and $v_{\mathrm{I},2}$), (middle-right column) LV DC-link capacitor voltage (v_{II}), and (right column) energy error distribution among C_{I}, C_{II} and total energy distribution ($\tilde{e}_{\mathrm{I}}$,$\tilde{e}_{\mathrm{II}}$, and $\tilde{e}_{\Sigma}$, respectively). From top to bottom, (top row) CC, (middle row) DC, and (bottom row) BC.

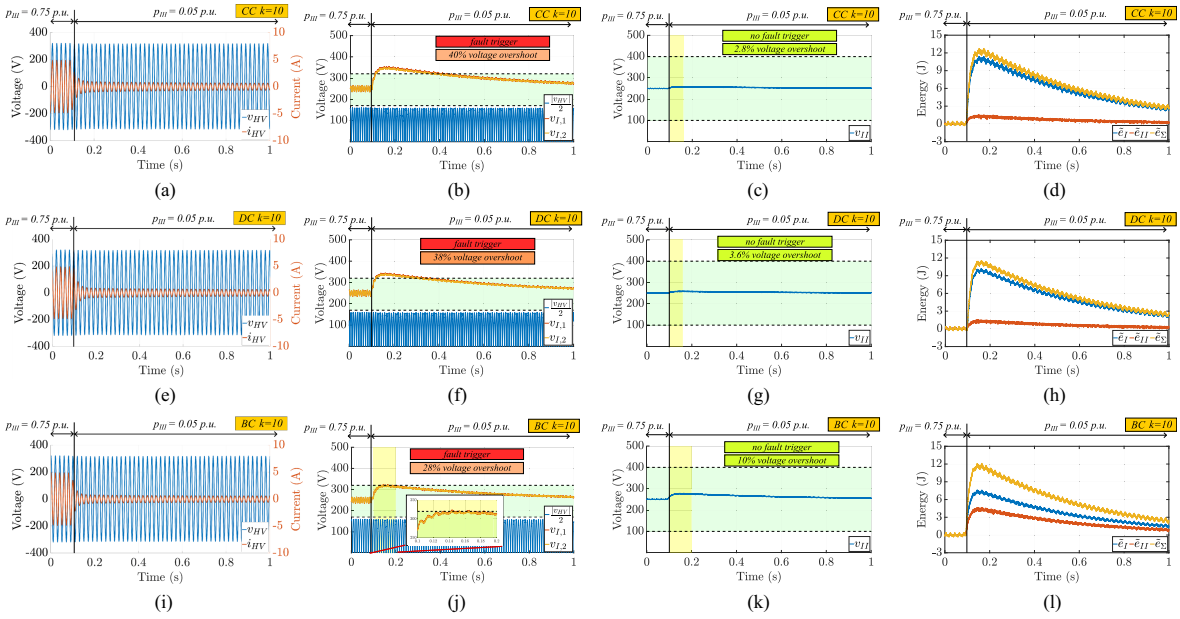

Fig. 10. Experimental results for a step load change from 0.75 to 0.05 p.u From left to right, (left column) HV grid voltage (v_{HV}) and HV grid current (i_{HV}) (middle-left column) HV DC-link capacitor voltages ($v_{\mathrm{I},1}$ and $v_{\mathrm{I},2}$), (middle-right column) LV DC-link capacitor voltage (v_{II}), and (right column) energy error distribution among C_{I}, C_{II} and total energy distribution ($\tilde{e}_{\mathrm{I}}$,$\tilde{e}_{\mathrm{II}}$ and $\tilde{e}_{\Sigma}$, respectively). From top to bottom, (top row) CC, (middle row) DC, and (bottom row) BC.

before, plus a 0.7 p.u increase in power, as shown in Fig. 11. Although the maximum and minimum limits of each dc-link voltage are defined, the system is allowed to continue operating for clarity. In practice, operations are disabled as soon as one of the limits is reached.

1) 0.5 P.u Load Step-Up: Fig. 9 presents the experimental results for a step change in load from 50 to 550 W. Fig. 9(a)–(d) displays the results using the CC. Specifically, Fig. 9(a) shows the HV grid voltage (v_{HV}) and HV grid current (i_{HV}). Fig. 9(b) depicts the variations in HV dc-link capacitor voltages ($v_{\mathrm{I},1}$ and $v_{\mathrm{I},2}$), highlighting the safe operating area in green. Fig. 9(c) illustrates the variations in LV dc-link capacitor voltage (v_{II}). Fig. 9(d) shows the total and individual incremental energies (i.e., $\tilde{e}_{\mathrm{I}}$, $\tilde{e}_{\mathrm{II}}$, and $\tilde{e}_{\Sigma}$). Similarly, from top to bottom, Fig. 9(e)–(h) and Fig. 9(i)–(l), display the results obtained using the DC and the BC, respectively.

For this load transient, Fig. 9(a) shows a 50% grid current overshoot when using the CC due to the overmodulation region

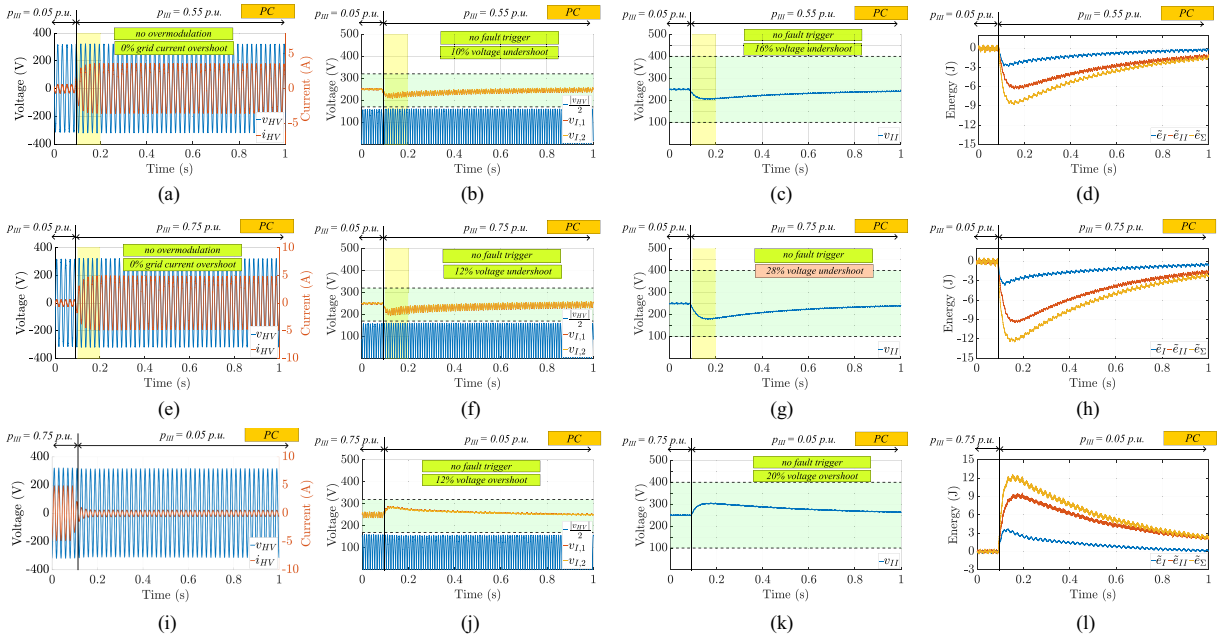

Fig. 11. Experimental results with DC and k designed based on (19). From left to right, (left column) HV grid voltage (v_{HV}) and HV grid current (i_{HV}) (middle-left column) HV DC-link capacitor voltages ($v_{\text{I},1}$ and $v_{\text{I},2}$), (middle-right column) LV DC-link capacitor voltage (v_{II}), and (right column) energy error distribution among C_{I}, C_{II} and total energy distribution ($\tilde{e}_{\text{I}}$, $\tilde{e}_{\text{II}}$, and $\tilde{e}_{\Sigma}$, respectively). From top to bottom, step load change from (top row) 0.05 to 0.55 p.u, (middle row) 0.05 to 0.75 p.u, and (bottom row) 0.75 to 0.05 p.u.

of operation. This overmodulation is caused by a 40% voltage drop on the HV dc-link capacitors from the reference voltage of 250 V, as seen in Fig. 9(b). With the chosen $k = 10$, only an 8% voltage drop is observed on the LV dc-link capacitor, as shown in Fig. 9(c). It should be noted that the 40% drop in the HV dc-link capacitor voltage would trigger the set fault limit ($V_{\text{I-min}} = 170$ V) and, in practical applications, discontinue the operation.

Similar results are observed with the DC in Fig. 9(e)–(h), with a 15% grid current overshoot, overmodulation region of operation, and a 40% drop in the HV dc-link voltages potentially triggering a shutdown in a practical system.

Using the BC, the overmodulation region of operation is avoided, as seen in Fig. 9(i), with improved dc-link voltage profiles showing a 26% voltage drop on the HV dc-link voltage and a 10% voltage drop on the LV dc-link voltage. However, the defined operational limits still trigger a fault.

2) 0.7 P.u Load Step-Down: Fig. 10 presents the results obtained for a reduction in load from 750 to 50 W, in a manner analogous to Fig. 9. Fig. 10(a)–(d) illustrates the operation using the CC. Fig. 10(b) shows a 40% voltage overshoot on the HV dc-link capacitors, while Fig. 10(c) indicates only a 2.8% voltage overshoot on the LV dc-link capacitor. Note that the HV dc-link capacitor voltage reaches the limit of $V_{\text{I-max}} = 320$ V, which will halt the system operation in practical applications.

The DC, as shown in Fig. 10(e)–(h), results in a 38% overshoot in the HV dc-link capacitor voltages and a 3.6% voltage overshoot in the LV dc-link capacitor voltage, depicted in Fig. 10(f) and (g), respectively. Similar to the CC, the DC will terminate the system operation in practical applications.

The BC, as depicted in Fig. 10(i)–(l), reveals a 28% overshoot in the HV dc-link capacitor voltages, as shown in Fig. 10(j), slightly exceeding the threshold limit and triggering a fault in practical applications.

3) DC With the Proposed Design Approach: Using (19) for the parameters in Table IV, results in $k = 1.37$ for $\{\tilde{e}_{\text{I}}, \tilde{e}_{\text{II}}\} \leq 0$ and $k = 1.26$ for $\{\tilde{e}_{\text{I}}, \tilde{e}_{\text{II}}\} > 0$. The corresponding experimental results are summarized in Fig. 11, where the top, middle, and bottom plots correspond to 0.5 p.u load step-up, 0.7 p.u load step-up, and 0.7 p.u load step-down, respectively. As it can be observed, fault triggers are entirely avoided for 0.5 p.u step changes in load by safely distributing energies based on the available reserve energies, as shown in Fig. 11(a)–(d). Remarkably, no overmodulation region is observed, preventing any grid-current overshoot. The improved energy distribution profile ensures continuous system operation. Notably, the proposed control design allows for safe energy distribution even with a 0.7 p.u step change in both ascending and descending directions, as seen in the middle and bottom plots of Fig. 11. With 0.7 p.u load step-up, a 12% voltage drop in the HV dc-link capacitors, achieved at the expense of a 28% voltage drop in the LV dc-link capacitor voltages is observed [see Fig. 11(e)–(h)]. With a 0.7 p.u load step-down, the HV dc-link capacitor voltages observes a 12% voltage overshoot in Fig. 11(j) at the expense of a 20% voltage overshoot in the LV dc-link capacitor voltages in Fig. 11(k). Nonetheless, the system remains safe within the specified limits.

4) Remarks: Two different plots, i.e., Fig. 12(a) and (b), are considered to illustrate the case of step-up load change and step-down load change, as the energy reserves change according

TABLE IV
EXPERIMENTAL SETUP PARAMETERS

System Parameters	Definitions	Values	p.u
	Stage I		
V_{HV}	HV grid voltage rms	230 V	1
P_{HV}	HV nominal power	1 kVA	1
L_{HV}	HV grid inductance	20 mH	0.1
N	Number of strings	2	
$C_{I,j}$	HV dc-link capacitance	190 μF	0.3
f_{acdc}	CHB switching frequency	18 kHz	
$V^*_{I,j}$	HV dc-link average voltage reference	250 V	1
	Stage II		
$L_{dab,j}$	DAB inductance	100 μH	
V^*_{II}	LV dc-link voltage reference	250 V	1
n	DAB transformer turns ratio	1:1	
C_{II}	LV dc-link capacitance	618 μF	0.1
f_{dcdc}	DAB switching frequency	50 kHz	
	Fault limits		
V_{I-min}	Undervoltage limit for $C_{I,j}(\geq \sqrt{2}V_{HV}/N)$	170 V	0.7
V_{I-max}	Overvoltage limit for $C_{I,j}$	320 V	1.3
V_{II-min}	Undervoltage limit for C_{II}	100 V	0.4
V_{II-max}	Overvoltage limit for C_{II}	400 V	1.6

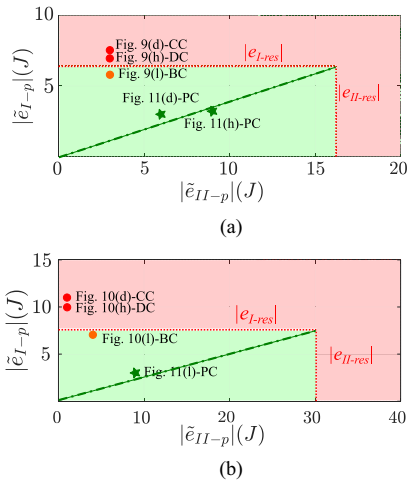

Fig. 12. SST internal incremental energy distribution charts illustrating reserved energies under different load conditions and using different control obtained from the experimental results in Figs. 8–10 for (a) load step-up and (b) load step-down.

to the load change direction. Thus, the peak energy changes observed for a load step-up, obtained from Figs. 9(d), (h) and (l), and 11(d) and (h), are plotted in Fig. 12(a). Similarly, peak energy changes observed for a load step-down, obtained from Figs. 10(d), (h) and (l), and 11(l), are plotted in Fig. 12(b). The green and red shaded areas are used to indicate the respective feasible regions. Note that, the average values are used to plot the energy distributions, neglecting the twice-grid-frequency capacitor voltage ripple on the HV capacitors. Thus, for the case of BC [see Figs. 9(l) and 10(l)], although the average values remain within the boundary limits of $|\tilde{e}_{\text{I-res}}|$, the presence of second-harmonic voltage ripple and calculation inaccuracies in energy limits—attributable to capacitor tolerance—cause the instantaneous voltage to occasionally reach the $V_{\text{I-max}}$ and $V_{\text{I-min}}$ levels in the experiments, as shown in Figs. 9(l) and 10(l). In contrast, the proposed reserved-energy-aided control method ensures sufficient operational margin to accommodate second-harmonic voltage ripple and capacitor tolerances.

As can be observed in Fig. 12, the green-starred points from the experimental results closely align with the optimal values (represented with the dot-dashed green line), validating the effectiveness of the proposed method. The proposed control, additionally, does not impact the steady-state operation. Thus, the steady-state efficiency for a given operating point remains the same, irrespective of the control strategy used. Having said that, the proposed control offers the lowest loss profile during the transient regime.

VI. CONCLUSION

This article has demonstrated the critical importance of effective energy management in SSTs to ensure stable operation within the prescribed feasible regions. By analyzing various control strategies for energy distribution, the limitations of CC methods to effectively distribute the energies among the dc-link capacitors is highlighted, showcasing the necessity for more analysis to choose control design parameters. The proposed concept of reserved energies enables the selection of optimal control gains for the DC strategy, thereby expanding the operating range of the SST. Experimental results validate the accuracy of the proposed analysis and demonstrate the improved dynamic performance of the proposed control design approach. Notably, the proposed SST effectively manages 0.7 p.u load changes in both ascending and descending directions without encountering overmodulation or overvoltage conditions. This stands in contrast to the conventional design approaches, which exhibit limitations even with 0.5 p.u load variations.

APPENDIX

The generalization of results obtained in Table II can be extended to $N = 3$ (3-string SST) as follows. Considering the CC law from Table I, the closed-loop state-space representation is obtained as

$$\dot{\tilde{x}} = \begin{bmatrix} \delta_1 & \delta_2 & \delta_2 & \frac{\beta_1}{3} & \delta_3 & \delta_4 & \delta_4 & \frac{\beta_2}{3} \\ \delta_2 & \delta_1 & \delta_2 & \frac{\beta_1}{3} & \delta_4 & \delta_3 & \delta_4 & \frac{\beta_2}{3} \\ \delta_2 & \delta_2 & \delta_1 & \frac{\beta_1}{3} & \delta_4 & \delta_4 & \delta_3 & \frac{\beta_2}{3} \\ 0 & 0 & 0 & -\beta_1 & 0 & 0 & 0 & -\beta_2 \\ 1 & 0 & 0 & 0 & 0 & 0 & 0 & 0 \\ 0 & 1 & 0 & 0 & 0 & 0 & 0 & 0 \\ 0 & 0 & 1 & 0 & 0 & 0 & 0 & 0 \\ 0 & 0 & 0 & 1 & 0 & 0 & 0 & 0 \end{bmatrix} \tilde{x}$$

$$+\begin{bmatrix}0\\0\\0\\-1\\0\\0\\0\\0\end{bmatrix}\tilde{p}_{\mathrm{III}} \tag{A1}$$

where the state variable matrix x is modified to include the additional state variables as $x = [e_{\mathrm{I},1}\ e_{\mathrm{I},2}\ e_{\mathrm{I},3}\ e_{\mathrm{II}}\ \int e_{\mathrm{I},1}\ \int e_{\mathrm{I},2}\ \int e_{\mathrm{I},3}\ \int e_{\mathrm{II}}]'$. The integral variables have been added to enforce zero steady-state error, and with

$$\begin{bmatrix}\delta_1\\\delta_2\\\delta_3\\\delta_4\end{bmatrix} = \frac{1}{3}\begin{bmatrix}-\alpha_1+2\xi_1\\-\alpha_1-\xi_1\\-\alpha_2+2\xi_2\\-\alpha_2-\xi_2\end{bmatrix}. \tag{A2}$$

Note that, assigning, $\xi_1 = -\alpha_1$ and $\xi_2 = -\alpha_2$, (A1) can be simplified as

$$\dot{\tilde{x}} = \begin{bmatrix}-\alpha_1 & 0 & 0 & \frac{\beta_1}{3} & -\alpha_2 & 0 & 0 & \frac{\beta_2}{3}\\ 0 & -\alpha_1 & 0 & \frac{\beta_1}{3} & 0 & -\alpha_2 & 0 & \frac{\beta_2}{3}\\ 0 & 0 & -\alpha_1 & \frac{\beta_1}{3} & 0 & 0 & -\alpha_2 & \frac{\beta_2}{3}\\ 0 & 0 & 0 & -\beta_1 & 0 & 0 & 0 & -\beta_2\\ 1 & 0 & 0 & 0 & 0 & 0 & 0 & 0\\ 0 & 1 & 0 & 0 & 0 & 0 & 0 & 0\\ 0 & 0 & 1 & 0 & 0 & 0 & 0 & 0\\ 0 & 0 & 0 & 1 & 0 & 0 & 0 & 0\end{bmatrix}\tilde{x} + \begin{bmatrix}0\\0\\0\\-1\\0\\0\\0\\0\end{bmatrix}\tilde{p}_{\mathrm{III}} \tag{A3}$$

which is in agreement with the result given in Table II of the revised manuscript, for the CC case. From the state-space representation in (A4), the following transfer functions can be obtained:

$$\left.\frac{E_{\mathrm{I},1}(s)}{P_{\mathrm{III}}(s)}\right|_{\mathrm{CC}} = \left.\frac{E_{\mathrm{I},2}(s)}{P_{\mathrm{III}}(s)}\right|_{\mathrm{CC}} = \left.\frac{E_{\mathrm{I},3}(s)}{P_{\mathrm{III}}(s)}\right|_{\mathrm{CC}} = \frac{\beta_1+\frac{\beta_2}{s}}{3(s+\alpha_1+\frac{\alpha_2}{s})} \tag{A4}$$

$$\left.\frac{E_{\mathrm{I}}(s)}{P_{\mathrm{III}}(s)}\right|_{\mathrm{CC}} = \left.\frac{\Sigma_{i=1}^{3}E_{\mathrm{I},i}(s)}{P_{\mathrm{III}}(s)}\right|_{\mathrm{CC}} = \frac{\beta_1+\frac{\beta_2}{s}}{s+\alpha_1+\frac{\alpha_2}{s}} \tag{A5}$$

$$\left.\frac{E_{\Sigma}(s)}{P_{\mathrm{III}}(s)}\right|_{\mathrm{CC}} = -\frac{1}{s+\alpha_1+\frac{\alpha_2}{s}}\left(\frac{\alpha_1+\frac{\alpha_2}{s}}{s+\beta_1+\frac{\beta_2}{s}}+1\right). \tag{A6}$$

where subscript CC denotes conventional control. Note that, (A5) and (A6) are in agreement with the results given in Table II of the revised manuscript, for the cc case. Similar conclusions can be drawn for the DC and BC.

Acknowledgment

The authors would like to acknowledge Energy Research Institute @ NTU, Singapore for providing financial support for covering article processing charges.

References

[1] X. She, A. Q. Huang, F. Wang, and R. Burgos, "Wind energy system with integrated functions of active power transfer, reactive power compensation, and voltage conversion," *IEEE Trans. Ind. Electron.*, vol. 60, no. 10, pp. 4512–4524, Oct. 2013.

[2] F. Ruiz, M. A. Perez, J. R. Espinosa, T. Gajowik, S. Stynski, and M. Malinowski, "Surveying solid-state transformer structures and controls: Providing highly efficient and controllable power flow in distribution grids," *IEEE Ind. Electron. Mag.*, vol. 14, no. 1, pp. 56–70, Mar. 2020.

[3] M. Liserre, G. Buticchi, M. Andresen, G. De Carne, L. F. Costa, and Z.-X. Zou, "The smart transformer: Impact on the electric grid and technology challenges," *IEEE Ind. Electron. Mag.*, vol. 10, no. 2, pp. 46–58, Jun. 2016.

[4] Q. Zhu, L. Wang, A. Q. Huang, K. Booth, and L. Zhang, "7.2-kV single-stage solid-state transformer based on the current-fed series resonant converter and 15-kV SiC MOSFETs," *IEEE Trans. Power Electron.*, vol. 34, no. 2, pp. 1099–1112, Feb. 2019.

[5] D. Dong, M. Agamy, J. Z. Bebic, Q. Chen, and G. Mandrusiak, "A modular SiC high-frequency solid-state transformer for medium-voltage applications: Design, implementation, and testing," *IEEE Trans. Emerg. Sel. Topics Power Electron.*, vol. 7, no. 2, pp. 768–778, Jun. 2019.

[6] C. Zhu, "High-efficiency, medium-voltage-input, solid-state-transformer-based 400-kW/1000V/400A extreme fast charger for electric vehicles," Delta Electronics Americas Ltd, Tech. Rep. EE-0008361, 2023.

[7] E. S. Lee, J. H. Park, M. Y. Kim, and J. S. Lee, "High-efficiency module design of solid-state transformers for railway vehicles," *IEEE Trans. Transport. Electrific.*, vol. 8, no. 1, pp. 98–120, Mar. 2022.

[8] Y. Kashihara, Y. Nemoto, W. Qichen, S. Fujita, R. Yamada, and Y. Okuma, "An isolated medium-voltage AC/DC power supply based on multil-cell converter topology," in *Proc. IEEE Appl. Power Electron. Conf. Expo.*, 2017, pp. 2187–2192.

[9] M. A. Hannan et al., "State of the art of solid-state transformers: Advanced topologies, implementation issues, recent progress and improvements," *IEEE Access*, vol. 8, pp. 19113–19132, 2020.

[10] A. Cervone, T. Wei, and D. Dujic, "Stability analysis of input-series/output-parallel solid-state transformers equipped with second-order harmonic active power filters," *IEEE Trans. Power Electron.*, vol. 39, no. 4, pp. 4127–4138, Apr. 2024.

[11] J. Ge, Z. Zhao, L. Yuan, and T. Lu, "Energy feed-forward and direct feed-forward control for solid-state transformer," *IEEE Trans. Power Electron.*, vol. 30, no. 8, pp. 4042–4047, Aug. 2015.

[12] T. Zhao, G. Wang, S. Bhattacharya, and A. Q. Huang, "Voltage and power balance control for a cascaded H-bridge converter-based solid-state transformer," *IEEE Trans. Power Electron.*, vol. 28, no. 4, pp. 1523–1532, Apr. 2013.

[13] S. Pugliese, M. Andresen, R. A. Mastromauro, G. Buticchi, S. Stasi, and M. Liserre, "A new voltage balancing technique for a three-stage modular smart transformer interfacing a DC multibus," *IEEE Trans. Power Electron.*, vol. 34, no. 3, pp. 2829–2840, Mar. 2019.

[14] G. Farivar, B. Hredzak, and V. G. Agelidis, "Decoupled control system for cascaded H-bridge multilevel converter based statcom," *IEEE Trans. Ind. Electron.*, vol. 63, no. 1, pp. 322–331, Jan. 2016.

[15] X. Mao, S. Falcones, and R. Ayyanar, "Energy-based control design for a solid state transformer," in *Proc. IEEE PES Gen. Meeting*, 2010, pp. 1–7.

[16] J. Nie, L. Yuan, W. Wen, R. Duan, B. Shi, and Z. Zhao, "Communication-independent power balance control for solid state transformer interfaced multiple power conversion systems," *IEEE Trans. Power Electron.*, vol. 35, no. 4, pp. 4256–4271, Apr. 2020.

[17] R. Sarda et al., "A control strategy for solid-state transformers with coupled load disturbance attenuation ability," *IEEE Trans. Power Electron.*, vol. 39, no. 4, pp. 4029–4041, Apr. 2024.

[18] Y. Zeng et al., "Active disturbance rejection control using artificial neural network for dual-active-bridge-based energy storage system," *IEEE Trans. Emerg. Sel. Topics Power Electron.*, vol. 11, no. 1, pp. 301–311, Feb. 2023.
[19] Q. Sun, Y. Li, D. Ma, Y. Zhang, and D. Qin, "Model predictive direct power control of three-port solid-state transformer for hybrid AC/DC zonal microgrid applications," *IEEE Trans. Power Del.*, vol. 37, no. 1, pp. 528–538, Feb. 2022.
[20] C. Ding, H. Zhang, Y. Chen, and G. Pu, "Research on control strategy of solid state transformer based on improved MPC method," *IEEE Access*, vol. 11, pp. 9431–9440, 2023.
[21] F. An, W. Song, B. Yu, and K. Yang, "Model predictive control with power self-balancing of the output parallel dab DC-DC converters in power electronic traction transformer," *IEEE Trans. Emerg. Sel. Topics Power Electron.*, vol. 6, no. 4, pp. 1806–1818, Dec. 2018.
[22] M. Ciobotaru, R. Teodorescu, and F. Blaabjerg, "A new single-phase PLL structure based on second order generalized integrator," in *Proc. 37th IEEE Power Electron. Specialists Conf.*, 2006, pp. 1–6.
[23] S. Shao et al., "Modeling and advanced control of dual-active-bridge DC-DC converters: A review," *IEEE Trans. Power Electron.*, vol. 37, no. 2, pp. 1524–1547, Feb. 2022.
[24] E. Rodriguez Ramos, R. Leyva, G. G. Farivar, C. D. Townsend, and J. Pou, "Capacitor condition monitoring for the low-capacitance statcom: An online approach," *IEEE Trans. Power Electron.*, vol. 37, no. 4, pp. 3697–3701, Apr. 2022.
[25] E. R. Ramos, R. Leyva, Q. Liu, G. G. Farivar, and J. Pou, "Capacitor condition monitoring method for low-capacitance statcoms: An online approach using the inherent second-harmonic oscillations," *IEEE Trans. Power Electron.*, vol. 38, no. 9, pp. 10559–10562, Sep. 2023.

Radhika Sarda (Graduate Student Member, IEEE) received the M.Sc. degree in energy engineering with a specialization in power electronics and drives from Aalborg University, Aalborg, Denmark, in 2018. She is currently working toward the Ph.D. degree in electrical engineering through the Interdisciplinary Graduate Programme with Nanyang Technological University, Nanyang, Singapore.

Her current research interest includes the control and optimization of solid-state transformers.

Ezequiel Rodriguez Ramos (Member, IEEE) was born in Tarragona, Spain, in 1994. He received the bachelor's degree in electrical engineering and the master's degree in engineering and technology of electronic systems (topping the 2012 and 2016 graduating cohorts as valedictorian) from Universitat Rovira i Virgili, Spain, in 2016 and 2017, respectively. He received the Ph.D. degree in electrical engineering from Nanyang Technological University (NTU), Nanyang, Singapore, in 2022.

He is currently serving as a Postdoctoral Research Fellow with the Energy Research Institute at NTU (ERI@N). In addition, he is the Director of the Power Electronics and Applications Research Lab with NTU (PEARL@NTU). Since January 2025, he has also been a Part-Time Lecturer for the MSc course EE6501: Power Electronic Converters at NTU. His research interests include control of power electronic converters, with an emphasis on modular multilevel converters for energy storage and FACTS applications.

Dr. Rodriguez is the recipient of the 2022 Best Thesis Award by the School of Electrical and Electronic Engineering, NTU, Singapore.

Glen G. Farivar (Senior Member, IEEE) received the B.Sc. degree in electrical engineering from the Nooshirvani Institute of Technology, Babol, Iran, in 2008, the M.Sc degree in power electronics from the University of Tehran, Tehran, Iran in 2011, and the Ph.D. degree in electrical engineering from the University of NSW Australia, Syndey, Australia in 2016.

He is currently working as a Lecturer with the University of Melbourne, Melbourne, VIC, Australia. He is a co-founder of SciLeap, which aims to promote research integrity, accessibility and openness. His research interests include renewable energy systems, high power convertors, energy storage, FACTS, and electric vehicles.

Josep Pou (Fellow, IEEE) received the B.S., M.S., and Ph.D. degrees in electrical engineering from the Technical University of Catalonia (UPC)-Barcelona Tech, Barcelona, Spain, in 1989, 1996, and 2002, respectively.

In 1990, he joined the faculty of UPC as an Assistant Professor, where he became an Associate Professor in 1993. From 2013 to 2016, he was a Professor with the University of New South Wales (UNSW), Sydney, Australia. From 2016 to 2024, he was a Professor with the Nanyang Technological University (NTU), Nanyang, Singapore, where he was co-Director of the Rolls-Royce @ NTU Corporate Lab and Cluster Director of Power Electronics at the Energy Research Institute with NTU (ERI@N). He is currently a Chair Professor with the City University of Hong Kong, Hong Kong. From 2001 to 2002, and 2005 to 2006, he was a Visiting Professor with the Center for Power Electronics Systems, Virginia Tech, Blacksburg. From 2012 to 2013, he was a Visiting Professor with the Australian Energy Research Institute, UNSW, Sydney. He has authored more than 500 published technical papers and has been involved in several industrial projects and educational programs in the fields of power electronics and systems. His research interests include modulation and control of power converters, multilevel converters, renewable energy, energy storage, power quality, HVdc transmission systems, and transportation electrification.

Prof. Pou is an Associate Editor of the IEEE JOURNAL OF EMERGING AND SELECTED TOPICS IN POWER ELECTRONICS. He was Co-Editor-in-Chief and an Associate Editor of the IEEE TRANSACTIONS ON INDUSTRIAL ELECTRONICS. He was the recipient of the 2024 IEEE PELS Sustainable Energy Systems Technical Achievement Award and the 2018 IEEE Bimal Bose Award for Industrial Electronics Applications in Energy Systems.

Howe Li Yeo He received the B.Eng. and M.Eng. degrees from NTU, in 2012 and 2018 respectively.

He is currently a Senior Engineer. He was previously a Research Associate with the Energy Research Institute@ Nanyang Technological University (NTU), Nanyang, Singapore.

His research interests include device characterization and wide bandgap semiconductors.

Vaisambhayana B. Sriram (Member, IEEE) received the B.Tech. degree in electrical engineering from REC, Kurukshetra, India, in 1995, the master's degree in power electronics from Bharathidasan University, Palkalaiperur, Tiruchirappalli, India, in 1997, and the Ph.D. degree in electrical engineering from the Indian Institute of Technology (IIT), Kharagpur, West Bengal, in 2003.

He is currently a Principal Research Fellow with Energy Research Institute @ NTU (ERI@N), Singapore, leading the advanced power electronics projects, with focus on medium voltage SiC-based solid-state transformers (SST). He has about 20 years of industrial experience, in the R & D of ABB India, GE India, GE Healthcare, USA, as an Architect in power electronics and the Energy Research Institute, NTU, Singapore. He is a co-founder and technical lead of a start-up Amperesand, in Singapore, that is productising medium-voltage SST. His research and design interests include Medium voltage cascaded converters, pulse power supplies, electromobility, grid connection and control of power converters.

Anshuman Tripathi received the M.Tech. degree specializing in industrial drives from IIT Kanpur, Kanpur, India, in 1999, and the Ph.D. degree in electrical engineering from the National University of Singapore, Singapore, in 2004.

He is currently the Senior Program Director with the Energy Research Institute @ NTU (ERI@N). He has two start-up companies dealing with energy storage systems and autonomous vehicles design solutions. His research interests include grid connection of large and remote wind and solar farms, grid codes and compliance, power hardware in the loop simulations for power network designs, electrical drive train designs for electric vehicles and hybrid energy storage for stationary and mobile applications.